Eur. Phys. J. A (2019) **55**: 51
DOI 10.1140/epja/i2019-12726-2

THE EUROPEAN PHYSICAL JOURNAL A

Regular Article – Experimental Physics

Measurement of the ^{58}Ni(n, p)^{58}Co and ^{58}Ni(n, 2n)^{57}Ni reaction cross-sections for fast neutron energies up to 18 MeV

Siddharth Parashari[1,a], S. Mukherjee[1,b], H. Naik[2], S.V. Suryanarayana[3], Rajnikant Makwana[1], B.K. Nayak[3], and N.L. Singh[1]

[1] Department of Physics, Faculty of Science, The M. S. University of Baroda, Vadodara - 390002, India
[2] Radiochemistry Division, Bhabha Atomic Research Center, Mumbai - 400085, India
[3] Nuclear Physics Division, Bhabha Atomic Research Center, Mumbai - 400085, India

Received: 24 September 2018 / Revised: 10 February 2019
Published online: 17 April 2019
© Società Italiana di Fisica / Springer-Verlag GmbH Germany, part of Springer Nature, 2019
Communicated by R.K. Bhandari

Abstract. The ^{58}Ni(n,p) and ^{58}Ni$(n,2n)$ reaction cross-sections were measured from threshold to 18 MeV neutron energies using the activation and off-line γ-ray spectroscopic technique. The quasi-monoenergetic neutron beam was generated using the ^{7}Li(p,n) reaction. The results from the present work were compared with those of the literature and with the evaluated data from different libraries, like ENDF-B/VII.1, JENDL-4.0, CENDL-3.1, and JEFF-3.3. Nuclear model codes, like TALYS-1.9 and EMPIRE-3.2.3-Malta, were also used for a better description of the present work and literature data. The uncertainties in the measured cross-section were evaluated using the covariance analysis. The present experimental results were found to be in good agreement with those of the literature and with the evaluated data. The nuclear model code TALYS-1.9 was found successful in reproducing the experimental data for both reactions. However, the EMPIRE-3.2.3-Malta model code was found to be able to reproduce only the trend of the ^{58}Ni(n,p) reaction excitation function. The present work provides a better insight on the comparison of both nuclear model codes. The present work is also essential for the production cross-section and the dose rate estimation of the medical isotope ^{58}Co.

1 Introduction

Neutron-induced reaction cross-section data are of prime interest for the advancement of the reactor technologies like Accelerated Driven Sub-critical systems (ADSs) [1,2] and International Thermonuclear Experimental Reactor (ITER) [3]. The reaction cross-section data are also vital for the dose estimation and to develop new economical routes for the production of rare medical isotopes. The isotopes of Nickel (Ni) have been extensively used over the years in different reactor grade steel alloys [4]. Ni is also used in the reactor cladding alloys like Zircaloy-2 [5]. Later, for the development of a less hydrogen producing cladding material, the composition of Ni and Fe has been limited in the Zircaloy-4 [5]. However, the physical and chemical properties of Ni make it a suitable candidate to be used in the ADSs and ITER. The operational energies for the ADSs and ITER are much higher than the present generation reactors. The interaction of high energy neutrons results in different (n,γ), (n,p), $(n,2n)$, (n,α), (n,np), $(n,\alpha n)$, $(n,3n)$ reactions, etc. The cross-section data for some of these reactions are important for the assessment of hydrogen production and for the estimation of the radiation damage to the reactor cladding and surrounding structural materials. Another aspect of the neutron-induced cross-section data with the structural materials is to estimate the production of medium and long lived isotopes. The (n,p) reaction with different Ni isotopes leads to the population of the four important medium-lived radio-isotopes ^{56,57,58,60}Co. Therefore, the study of the neutron-induced reaction cross-sections becomes essential for the fast neutron energies up to 20 MeV [4]. The (n,p) reaction channel of the ^{58}Ni produces the ^{58}Co isotope, which has several medical applications. The most important is its use as a trace element for the absorption of vitamin B12 in the human body [6].

There are different nuclear model codes available for the reproduction of the neutron reaction cross-sections data. Among those, we have found the TALYS-1.9 [7] and the EMPIRE-3.2.3 [8] successful for the comparison of the nuclear data from medium to fast neutron energies. In the present work, both codes were compared and tested for the present and literature data. The different level density

[a] e-mail: siddharthparashri5@gmail.com
[b] e-mail: sk.mukherjee-phy@msubaroda.ac.in

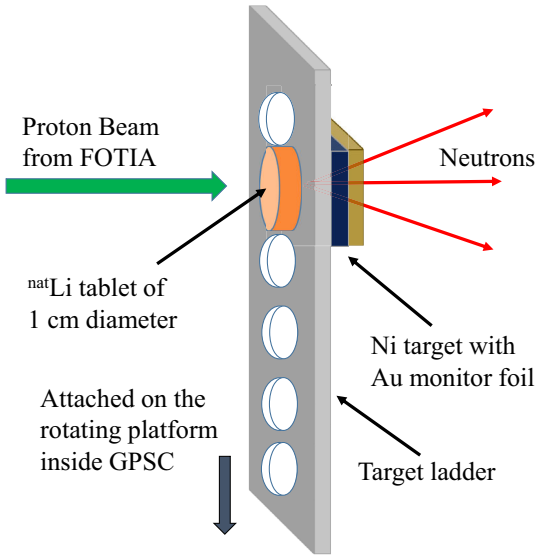

Fig. 1. (Color online) Schematic diagram of the experimental setup used for irradiations at FOTIA.

models present in the codes were also tested in order to find a better description of the reaction cross-section data.

The compilation of the EXchange FORmat (EXFOR) [9] data library suggests that a sufficient amount of nuclear cross-section data are present for both ^{58}Ni(n,p) and ^{58}Ni$(n,2n)$ reactions in the literature [4, 10–46]. It can also be seen that the cross-section data from different authors are in good agreement around the 14 MeV neutron energies. However, data contain minor discrepancies around the 8 MeV for (n,p) reaction and above 16 MeV for both (n,p) and $(n,2n)$ reactions. The disagreement among the literature data may be attributed to the use of different monitor reactions. Since measurements are relative to the monitor cross-sections and detector efficiencies, the monitor cross-sections also contribute to the uncertainty in the measured data. The error propagation method is very useful to calculate the uncertainties as well as the correlations among the measured data. In the present work, a detailed covariance analysis was performed to calculate the uncertainties in the measured data as a composition of the errors from each quantity taken into account for the calculations. The present work provides a clear insight into the TALYS-1.9 [7] and EMPIRE-3.2.3-Malta [8] nuclear model codes and the importance of error propagation in the neutron-induced nuclear reaction cross-section data. Also the measured data are of particular interest in medical applications of the ^{58}Co isotope.

2 Experimental details

The present experimental work was performed in two sets using different accelerators. The first set of experiments was performed at the Folded Tandem Ion Accelerator (FOTIA) at the Bhabha Atomic Research Center, Mumbai, India, using the activation technique followed by off-line γ-ray spectroscopy. The optimum proton energy at FOTIA is 6 MeV. We have irradiated two samples of 0.025 mm thick nickel (Ni) metal foil with the neutrons generated using the 5.4 and 5 MeV proton energies. The neutrons were generated using the ^{7}Li(p,n) reaction with the proton energies of 5.4 and 5 MeV. A tablet of natural lithium fluoride (^{nat}LiF) with a diameter of $\approx$ 1 cm and a thickness of 2 mm was used in both irradiations. It was placed on the front side of the target ladder. The Ni and Au targets were separately wrapped in a thin Al foil ($\approx$ 0.015 mm) and placed together at the back of the target ladder. The target ladder was mounted inside the general purpose scattering chamber (GPSC) for both irradiations. A schematic diagram of the irradiation setup is shown in fig. 1. Separate foils of Gold (Au) of thickness 0.025 mm were used together with the Ni foils to measure the incoming neutron flux. Irradiations were carried out for about 5–6 hours to accumulate sufficient radioactivity in the samples. After each irradiation the samples were allowed to cool for about 20 minutes to reduce the radioactive dose to a safe and permissible limit. The samples were then mounted on separate perspex plates and taken for γ-ray counting. An HPGe detector (detector 1) together with the PC based 4K multichannel analyzer was used for the γ-ray counting of the samples. The mounted samples were placed one at a time at 1 cm distance from the end cap of the HPGe detector and were counted for an appropriate time to reduce statistical uncertainty. The dead time of the detector system during the counting was $< 2\%$. The HPGe detector was pre-calibrated with a standard ^{152}Eu source. The resolution of the detector during the counting was measured as 2.0 keV for 1332 keV of ^{60}Co.

The second set of the experiment was carried out by using the 14UD Bhabha Atomic Research Center-Tata Institute of Fundamental Research (BARC-TIFR) Pelletron facility in Mumbai, India. The neutrons were generated by using the ^{7}Li(p,n) reaction with the proton beam of 8, 16, and 19 MeV energies. A (^{nat}Li) metal target of thickness 6.8 mg/cm^2 was used in between the two tantalum (Ta) foils of different thicknesses. A Ta foil of thickness 4 mg/cm^2 was used at the front of the Li foil and another 0.1 mm thick Ta foil was used at the back of Li to prevent the protons from hitting the samples. Behind Ta-Li-Ta stack, a Ni metal foil (0.1 mm) was placed at a distance of 2.1 cm, aligned at zero degrees with respect to the proton beam for each irradiation. Aluminum and indium metal (monitor) foils of thickness 0.1 mm each were placed together with each Ni (sample) to evaluate the neutron flux. The area of both the monitor and the sample foils was taken as 1×1 cm^2 in order to avoid the area corrections in the flux. All the sample and monitor foils were separately wrapped in a thin Al foil ($\approx$ 0.015 mm) to avoid the cross contamination among the irradiated samples. The irradiations were carried out at the 6-meter irradiation port of the main beam line at the Pelletron. This port is suitable for irradiations, which require high proton flux. A collimator of 6 mm diameter was used to get a circular shaped proton beam. A schematic diagram of the experimental arrangement of the stack used for irradiation is shown in fig. 2. The irradiation for each sample was carried out for

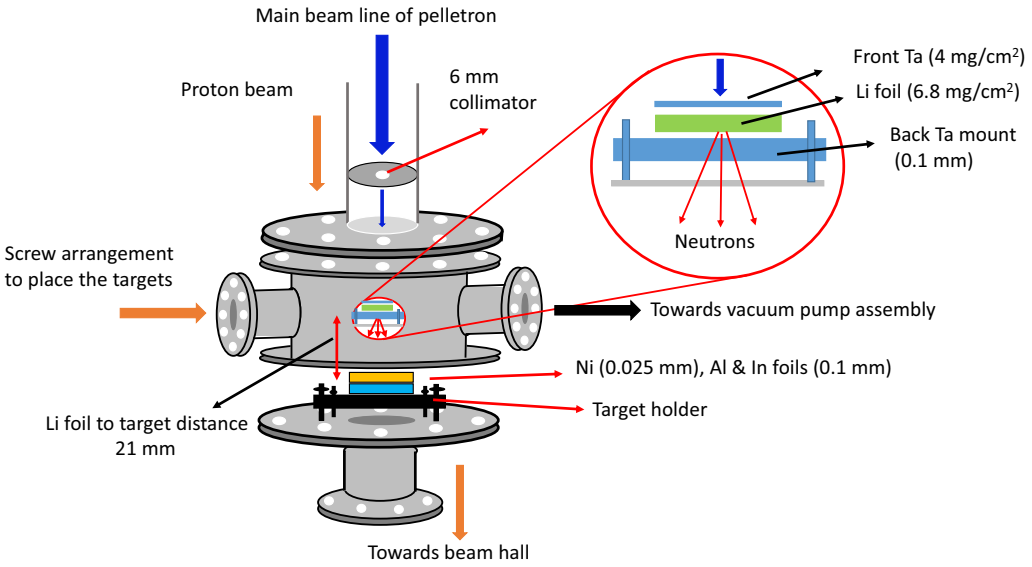

Fig. 2. (Color online) A typical arrangement of the experimental setup used for the irradiations at 14UD Pelletron.

Table 1. The summary of the present experimental work.

Experimental details	Set 1	Set 2
Accelerator used	FOTIA (BARC, Mumbai)	14UD Pelletron (BARC-TIFR, Mumbai)
Proton energies	5.4 and 5	8, 16, and 19
neutron energies	2.97 and 3.37	5.99, 13.97 and 16.99
Sample reactions	^{58}Ni$(n,p)^{58}$Co	^{58}Ni$(n,p)^{58}$Co and ^{58}Ni$(n,2n)^{57}$Ni
Monitor reactions	^{197}Au$(n,\gamma)^{198}$Au	^{115}In$(n,n')^{115m}$In and the ^{27}Al$(n,\alpha)^{24}$Na
Sample thickness	0.025 mm	0.025 mm
Monitor thickness	0.025 mm	0.1 mm for both In and Al
Sample weight	127.4 and 113.1 mg	$\approx$ 22 mg
Monitor weight	107 and 138.7 mg	$\approx$ 140 mg (In) and $\approx$ 30 mg (Al)
Sample dimensions	1.1×1.2, 1.25×0.75 cm^2	1×1 cm^2
Monitor dimensions	1.0×0.4, 1.1×0.7 cm^2	1×1 cm^2

about 7–8 hours to build up sufficient activity which was subsequently counted for an appropriate time by using a pre-calibrated 80 cm^3 single crystal HPGe detector (detector 2) coupled to a PC based multi-channel analyzer. The HPGe detector was calibrated with a standard ^{152}Eu source and the resolution of the detector during counting was measured as 1.82 keV for 1332 keV γ-ray of ^{60}Co. The proton current was kept constant during irradiations to avoid large uncertainties in the proton flux. The dead time of the detector system was kept as $< 2\%$ for each counting. For the sake of clarity, a brief summary of the experiments is provided in table 1.

3 Data analysis

3.1 Calculations for neutron spectra

The proton energies of 5, 5.4, 8, 16, and 19 MeV were used in the present work for irradiation. A ^{nat}LiF tablet wrapped in a thin Al foil was used for the 5 and 5.4 MeV proton energies and a Li metal foil was used for 8, 16, and 19 MeV protons. The degradation of the proton energy in the LiF tablet and the Ta-Li-Ta stack was calculated using SRIM [47]. As for the representation, the neutron spectra generated from 5.4 and 19 MeV protons are shown in fig. 3. The natural lithium consists of ^{6}Li and ^{7}Li isotopes with abundances of 7.42% and 92.58%, respectively [48]. A number of reactions take place when the protons interact with the natural lithium target. The most prominent is the production of ground state of ^{7}Be from the ^{7}Li(p,n) reaction, which has a threshold energy of 1.88 MeV, whereas the threshold energy for its first excited state is 2.38 MeV. The ground and the first excited states of ^{7}Be contribute to the n_0 and the n_1 group of neutrons. Above the proton energy of 4.5 MeV, the fragmentation of ^{8}Be leads to a continuous distribution of neutrons besides n_0 and n_1 groups. Liskien *et al.* [49] and Meadows *et al.* [50] have calculated the branching ratios

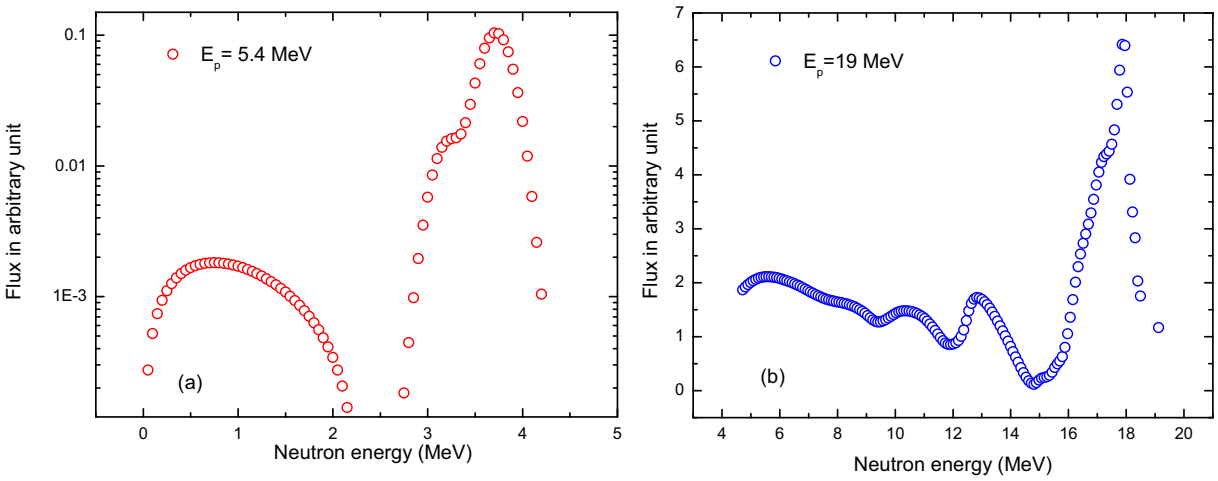

Fig. 3. (Color online) The ^{7}Li(p, n) reaction generated neutron spectra at 5.4 [52] and 19 [53] MeV proton energies.

of n_0 and n_1 group on neutrons originating from ^{7}Be up to 7 MeV proton energies. In addition to this, Poppe *et al.* [51] have given the branching ratio to the ground and first excited state of ^{7}Be for 4.2–26 MeV proton energies. Meadows and Smith [50] have also provided parameterized experimental neutron distribution from the break-up channels. Based on the description provided in the literature [49–51], the neutron spectra were calculated for the proton energies of 5, 5.4, 8, 16, and 19 MeV. The n_0 and n_1 group contributes to the main peak of the neutron distribution, however, the break-up channels contribute to the tail part as can be seen from fig. 3. A detailed discussion on the generation of neutron spectra is also provided in our earlier publications [52–54]. Similar neutron spectra were also used by other groups [10, 11, 13] and the reported cross-sections were found in agreement with the literature and theoretical data for the respective case of study. For the sake of the comparison, MCNP6.1 calculations were preformed by Katovsky (Department of Electrical Power Engineering, Brno University of Technology, Brno, Czech Republic) for the neutron spectrum generation using the defined geometry of the target assembly for the given neutron energies of 5.4 and 19 MeV protons. The simulated spectra were found in agreement with the theoretical reproductions from the previous works [49–51]. Minor discrepancies, however, were found among the results. A rough estimation of the neutron flux using the simulated spectra was found in agreement with the flux used in the present workwithin the uncertainty of $\approx 3\%$. As the proton energy increases, more channels open up and contribute to the neutron spectra and hence result in a broad quasi-monoenergetic peak along with the long continuum towards the low energy neutrons. This lower energy continuum is referred to as the tail region, consisting of lower neutron energies, which also contribute in the reaction cross-section. Therefore, it is necessary to remove the contribution of reaction cross-section arising from the tail part of the neutron spectrum. This correction can be done by considering spectral average cross-sections [53,54] as described in the next section. The uncertainty due to the total neutron flux were incorporated in the covariance analysis as the uncertainty in the weighted cross-sections of monitor reaction from the ENDF-B/VII.1 and EXFOR library. The errors in the neutron energies for the n_o and n_1 group of neutrons (main peak of the distributions) were calculated by using the SRIM [47] code and represented as the error on the energy axis.

3.2 Measurement of the ^{58}Ni(n, p) and ^{58}Ni(n, 2n) reaction cross-sections

The neutron spectra generated using the methodology described above as well as in ref. [54] were used for the calculation of the neutron flux. In the present measurement, we have used the ^{197}Au$(n, \gamma)^{198}$Au, ^{115}In$(n, n')^{115m}$In and the ^{27}Al$(n, \alpha)^{24}$Na reactions as the flux monitor. The γ-lines of energies, 411.8 (95.62%), 336.2 (45.0 $\pm$ 0.1%), and 1368.7 (89.43 $\pm$ 0.23%) keV [55], respectively, were used for the flux calculations. The ^{197}Au$(n, \gamma)^{198}$Au and ^{115}In$(n, n')^{115m}$In reactions were used for the ^{58}Ni(n, p) reaction, while the ^{27}Al$(n, \alpha)^{24}$Na reaction was used for the ^{58}Ni$(n, 2n)$ reaction as it has a threshold of 3.249 MeV. The typical γ-spectra recorded using the HPGe detector for monitor reactions are shown in figs. 4(a)–(c). The monitor reactions were chosen according to the (n, p) and $(n, 2n)$ reaction thresholds. To obtain the flux value in each case, a spectral weighted cross-section ($\langle\sigma_W\rangle$) was first calculated for the monitor reaction using the evaluated and experimental cross-sections taken from the ENDF-B/VII.1 [56] and EXFOR [57] data library. The evaluated cross-sections from the ENDF-B/VII.1 [56] library were taken for ^{197}Au$(n, \gamma)^{198}$Au and ^{27}Al$(n, \alpha)^{24}$Na reactions. However, We have used the EXFOR (experimental results) data for the ^{115}In$(n, n')^{115m}$In monitor reaction. The ENDF library data are around 10% larger than the experimentally observed values by a large number of groups. Since we have used Al as well as In during the same irradiation, the flux should come out to be in agreement by using both reactions. The neutron fluxes using both monitor reactions agree when we use the EXFOR data but the neutron flux by In changes by the or-

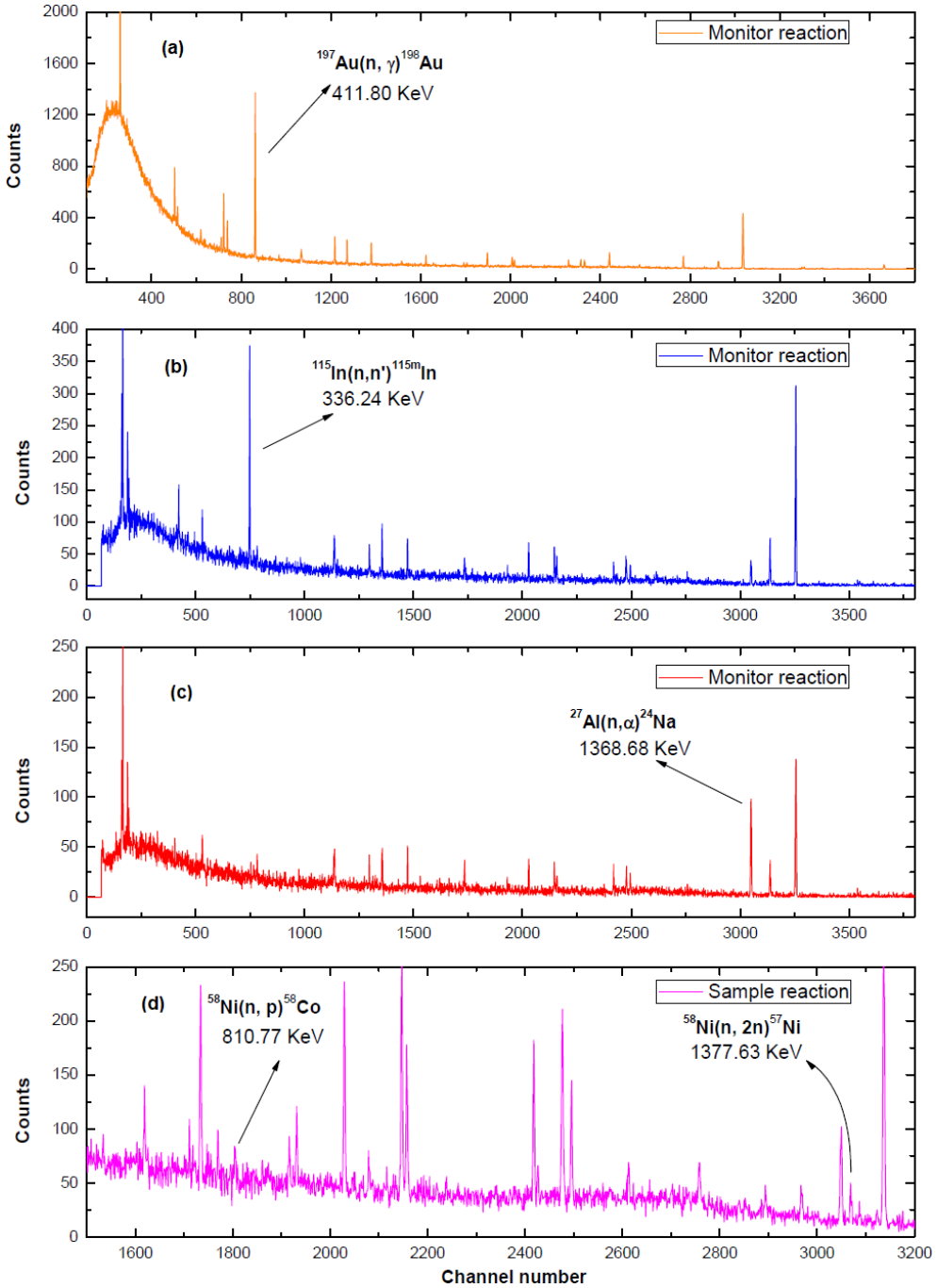

Fig. 4. (Color online) The typical recorded spectra for (a) $^{197}\mathrm{Au}(n,\gamma)^{198}\mathrm{Au}$, (b) $^{115}\mathrm{In}(n,n')^{115m}\mathrm{In}$, (c) $^{27}\mathrm{Al}(n,\alpha)^{24}\mathrm{Na}$, and (d) $^{58}\mathrm{Ni}(n,p)$, $(n,2n)$ reactions.

der of 10 with respect to the flux calculated using the Al monitor reaction. The ENDF and the EXFOR data for Al reaction agree throughout the energy range. Therefore, we have used the EXFOR data for In to match the flux from both monitor reactions. The following relation was used to calculate the weighted monitor cross-sections:

$$\langle \sigma_W \rangle = \frac{\sum_{E_i} \phi_i \sigma_i}{\sum_{E_i} \phi_i}, \quad (1)$$

where ϕ_i and σ_i are the neutron flux and corresponding monitor reaction cross-section respectively, taken from ENDF/B-VII.1 [9]. The total neutron flux has been calculated by using the following expression:

$$\langle \Phi \rangle = \frac{C_{obs}\lambda(\frac{CL}{LT})}{N_0\langle \sigma_W \rangle I_\gamma \epsilon (1-e^{-\lambda t_i})(e^{-\lambda t_c})(1-e^{-\lambda LT})}, \quad (2)$$

where C_{obs} is the observed counts for respective γ-ray of products from monitor reaction, CL and LT are the

Table 2. Nuclear spectroscopic properties of products from monitor and sample reactions taken from ref. [55].

Reaction	Threshold (Q-value) (MeV)	$T_{1/2}$	Decay mode	E_γ (keV)	I_γ (%)
^{197}Au$(n,\gamma)^{198}$Au	– (0.65)	2.6941 ± 0.0002 d[(a)]	$\beta^-(100\%)$	411.8	95.62
^{27}Al$(n,\alpha)^{24}$Na	3.249	14.997 ± 0.012 h[(a)]	$\beta^-(100\%)$	1368.7	89.43 ± 0.23
^{115}In$(n,n')^{115m}$In	–	4.486 ± 0.004 h[(a)]	$IT(95.00\%)$ $\beta^-(5.00\%)$	336.2	45.9 ± 0.1
^{58}Ni$(n,p)^{58}$Co	– (0.4)	70.86 ± 0.06 d[(a)]	$\varepsilon(100\%)$	810.7	99.45
^{58}Ni$(n,2n)^{57}$Ni	12.428	35.60 ± 0.06 h[(a)]	$\varepsilon(100\%)$	1377.6	81.70 ± 0.24

[(a)] d ⟶ days, h ⟶ hours.

clock time and the live time for the counting of the spectrum, t_i, t_c are the irradiation and the cooling time of the samples, λ is the decay constant ($\lambda = 0.693/t_{1/2}$), I_γ is the branching ratio for the respective γ-ray taken from ref. [55], N_0 is the total number of target nuclei in the sample and ϵ is the detector efficiency. All the spectroscopic data used in the calculation of flux is given in table 2. The ^{27}Al$(n,\alpha)^{24}$Na monitor reaction and the sample $(n,2n)$ reaction has different threshold energies; 3.249 and 8.37 MeV, respectively. The sample $(n,2n)$ reaction cross-sections are not sensitive to neutrons below 8.37 MeV. However, the monitor reaction is sensitive to neutrons from 3.249 MeV to the maximum available energy. Therefore, the absolute neutron flux contribution to the ^{58}Ni$(n,2n)$ reaction was calculated by taking the area under the neutron distributions from threshold to maximum neutron energy for sample reaction. The detailed method for the flux correction has also been described earlier [54].

A typical recorded spectrum for the sample reactions with the γ-lines used in the cross-section measurement is shown in fig. 4(d). The ^{58}Ni(n,p) reaction channel results in ^{58}Co, which has a half-life of 70.86 ± 0.06 days. The (n,p) reaction cross-sections were measured using the counting statistics of γ-line of 810.76 (99.45%) keV. Similarly, the ^{58}Ni$(n,2n)^{57}$Ni reaction channel was measured using the 1377.63 ($81.70 \pm 0.24\%$) keV γ-line following the half-life of 35.60 ± 0.06 hours. Equation (2) now can be rewritten for the calculation of both (n,p) and $(n,2n)$ reaction cross-sections $\langle\sigma_R\rangle$ as

$$\langle\sigma_R\rangle = \frac{C_{obs}\lambda(\frac{CL}{LT})}{N_0\langle\Phi\rangle I_\gamma\epsilon(1-e^{-\lambda t_i})(e^{-\lambda t_c})(1-e^{-\lambda LT})}, \quad (3)$$

where σ_R is the reaction cross-section, C_{obs} are the delineated counts from the $(n,2n)$ reaction channel only and the other symbols have the same meanings as in eq. (2). Neutron flux (Φ) calculated from eq. (2) is used in (3). All the spectroscopic data for the calculations were taken from NuDat [10] and are given in table 2.

4 Covariance analysis

The covariance (correlation) analysis is a mathematical tool which can help in the best estimation of uncertainty along with the cross-correlations among different measured quantities. In the present work, the reaction cross-sections for a particular experimental set were measured at different neutron energies using the common detector setup. Therefore, the reaction cross-sections are correlated with the detector efficiencies. Besides the counts from the recorded γ-ray spectra, various parameters with definite uncertainties were also taken into consideration for the calculations of the reaction cross-sections. The errors from all these quantities must be propagated into the final results. Therefore, by using this technique, we were able to transfer the uncertainties from all the different sources into the results. In this method we have first calculated the uncertainties in the detector efficiencies then using those values we have obtained the correlations among the cross-sections. The details of the technique used are given in the following subsections.

4.1 Uncertainty in the detector efficiencies

The efficiency of the HPGe detector was determined by using the standard ^{152}Eu γ-ray source. The absolute value of efficiencies of the detector for different γ-ray energies are geometry-dependent and can be given by the relation,

$$\varepsilon = K_c \frac{C}{N_0 I_\gamma e^{-\lambda T} \triangle t}, \quad (4)$$

where ε is the geometry dependent efficiency, C is the observed count rate for a particular γ-line of interest with absolute intensity I_γ. T is the time interval between the date of preparing the ^{152}Eu γ-ray source, $\triangle t$ is the counting time, and observation, N_0 is the absolute disintegration rate at the date of preparing the ^{152}Eu γ-ray source and K_c is the summing correction factor calculated using the EFFTRAN code [58].

The detector efficiency can be written as a function of the four attributes, $\varepsilon = f(C, N_0, I_\gamma, T_{1/2})$, and can be expanded as

$$\left(\frac{\triangle\varepsilon_i}{\varepsilon_i}\right)^2 = \left(\frac{\triangle C_i}{C_i}\right)^2 + \left(\frac{\triangle N_o}{N_0}\right)^2 + \left(\frac{\triangle I_{\gamma_i}}{I_{\gamma_i}}\right)^2 + (t \triangle \lambda)^2, \quad (5)$$

where $\triangle C_i$, $\triangle N_o$, $\triangle I_{\gamma_i}$ are the uncertainties in C_i, N_o, I_{γ_i}, respectively, and $\triangle\lambda$ is the uncertainty in the decay

Table 3. Partial uncertainties in the efficiency of detector 1 (sert 1) used at the BARC FOTIA facility.

Energy	Partial uncertainty ($\times 10^4$) due to attributes				Total uncertainty ($\times 10^4$)
(KeV)	$r = 1(C)$	$r = 2(I_\gamma)$	$r = 3(N_0)$	$r = 4(T_{1/2})$	$(\sigma_{\varepsilon_{ii}})$
121.8	0.19244	0.844	0.42829	0.00399	0.96582
244	0.29325	0.521	0.26438	0.00246	0.65371
344	0.14519	0.449	0.22785	0.00212	0.52402
778.9	0.16161	0.27039	0.13721	0.00128	0.34359
1112	0.12753	0.19908	0.10102	0.00094	0.25711
1408	0.10186	0.174	0.08829	0.00082	0.22011

Table 4. Partial uncertainties in the efficiency of detector 2 (set 2) used at the BARC-TIFR Pelletron facility.

Energy	Partial uncertainty ($\times 10^3$) due to attributes				Total uncertainty ($\times 10^3$)
(KeV)	$r = 1(C)$	$r = 2(I_\gamma)$	$r = 3(N_0)$	$r = 4(T_{1/2})$	$(\sigma_{\varepsilon_{ii}})$
121.8	0.81566	1.01983	1.15536	0.00483	1.74363
244	0.78326	0.62054	0.70301	0.00294	1.22180
443.9	0.68761	0.43059	0.48782	0.00204	0.94668
964	0.26486	0.22077	0.25011	0.00104	0.42597
1112	0.25839	0.19907	0.22552	0.00094	0.39656
1408	0.18161	0.16532	0.18729	0.00078	0.30886

constant λ which can be defined as, $\triangle\lambda = \ln 2 \triangle T_{1/2}/T_{1/2}^2$. The covariance matrix for detector efficiencies can now be generated as

$$(V_\varepsilon)_{ij} = \sum_r e_{ir} S_{ijr} e_{jr}, \tag{6}$$

where e_{ir}, e_{jr} are the diagonal matrices and S_{ijr} are the micro correlation matrices, which may be given as the $(n \times n)$ unity matrix for the uncorrelated elements and a $(n \times n)$ square matrix with each element as "1" for completely correlated cases. S_{ijr} can also be a $(n \times n)$ matrix with elements $0 < S_{ijr} < 1$ for partially correlated cases. The partial uncertainties for experiment set 1 and 2 related to the four attributes are given in tables 3 and 4, respectively. The covariance matrices for both sets of experiments, generated by using eqs. (5) and (6) are given in tables 5 and 6, respectively. The efficiencies and the relative correlations for the γ lines used for the cross-section calculations were generated using the model equation

$$\ln \varepsilon_i = \sum_m p_m (\ln E_i)^{m-1}, \tag{7}$$

where ε_i are the efficiencies considered in the cross-section calculations, p_m are the fitting parameters of order m and E_i are the corresponding γ-ray energies. Equation (7) can be written as $Z = AP$, with fitting parameters $\hat{P}$ given as

$$\hat{P} = V_{\hat{P}}(A' V_z^{-1} Z), \tag{8}$$

where matrix V_z can be obtained using, $(V_z)_{ij} = \frac{(V_\epsilon)_{ij}}{\langle \epsilon_i \rangle \langle \epsilon_j \rangle}$, $V_{\hat{P}}$ is the covariance matrix and the goodness of the fit can be calculated by, $\chi_m^2 = (Z - AP)' V_z^{-1} (Z - AP)$. Using eq. (8) we obtain the fitting parameters as $\hat{P} = (-6.1254, -0.79281, 0.17388, 0.40937, 0.13875)$ with a value of $\chi_m^2 = 2.35$, for set 1 and $\hat{P} = (-0.38370, -0.8694, 0.1693, 0.3208, -0.1)$ with a value of $\chi_m^2 = 0.72$, for set 2. The calculated efficiencies and the corresponding correlation matrix for the characteristic γ-lines used for the calculation of the reaction cross-sections are given in tables 7 and 8 for set 1 and 2, respectively.

Table 5. Covariance matrix ($V_\varepsilon \times 10^6$) for the detector 1 efficiencies.

0.009328					
0.001132	0.004273				
0.000976	0.000602	0.002746			
0.000588	0.000363	0.000313	0.001181		
0.000433	0.000267	0.000023	0.000139	0.000661	
0.000378	0.000233	0.000201	0.000121	0.000089	0.000485

4.2 Uncertainty in the measured reaction cross-sections

Since the sample reaction cross-sections $\langle \sigma_s \rangle$ were normalized with respect to the monitor reaction cross-sections $\langle \sigma_m \rangle$, the ratio measurement technique [59] was used in the covariance analysis. The sample reaction parameters are denoted with suffix "s" and the monitor reaction parameters with suffix "m". Using eqs. (2) and (3), we can

Table 6. Covariance matrix ($V_\varepsilon \times 100$) for the detector 2 efficiencies.

0.0030938					
0.0008305	0.0015126				
0.0005763	0.0003507	0.0009057			
0.0002955	0.0001798	0.0001248	0.0001840		
0.0002664	0.0001621	0.0001125	0.0000577	0.0001593	
0.0001346	0.0001346	0.000934	0.0000479	0.0000432	0.0000968

write

$$\langle \sigma_s \rangle = \langle \sigma_m \rangle \frac{C_s N_{0_m} \varepsilon_m I_{\gamma_m} f_{\lambda_m}}{C_m N_{0_s} \varepsilon_s I_{\gamma_s} f_{\lambda_s}}, \tag{9}$$

with the time factor f defined as

$$f = \left(1 - e^{-\lambda t_i}\right)\left(e^{-\lambda t_c}\right)\left(1 - e^{-\lambda LT}\right)/\lambda. \tag{10}$$

Using the number of target nuclei N_0 (given by $N_0 = (MN_A a)/A$, where M is the sample weight, N_A is the Avogadro number, a is the isotopic abundance and A is the atomic mass) we can write eq. (9) as

$$\langle \sigma_s \rangle = \langle \sigma_m \rangle \frac{C_s M_m a_m A_s \varepsilon_m I_{\gamma_m} f_{\lambda_m}}{C_m C_s M_s a_s A_m \varepsilon_s I_{\gamma_s} f_{\lambda_s}}. \tag{11}$$

The partial uncertainties due to each attribute in the above equation can be propagated directly to the sample cross-section $\langle \sigma_s \rangle$ using the quadratic sum formula. The partial uncertainty in the decay constant is related to $\langle \sigma_s \rangle$ by an exponential function, therefore, the uncertainty in the time factor "f" must be propagated as

$$\left(\frac{\triangle f}{f}\right)^2 = \left(\frac{\lambda t_i e^{-\lambda t_i}}{1 - e^{-\lambda t_i}} - \lambda t_c + \frac{\lambda (LT) e^{-\lambda (LT)}}{1 - e^{-\lambda (LT)}} - 1\right)^2 \left(\frac{\triangle \lambda}{\lambda}\right)^2, \tag{12}$$

with the relative sensitivity given by

$$s_{f\lambda} = \left(\frac{\lambda t_i e^{-\lambda t_i}}{1 - e^{-\lambda t_i}} - \lambda t_c + \frac{\lambda (LT) e^{-\lambda (LT)}}{1 - e^{-\lambda (LT)}} - 1\right). \tag{13}$$

The uncertainty in the detector 2 efficiencies (which were found to be around 2 %) can be reduced further for both the sample and the monitor by introducing $\eta_{m,s} = \varepsilon_m/\varepsilon_s$ [59] with the partial uncertainty given as $\frac{\triangle \eta_{m,s}}{\eta_{m,s}} = \mathrm{var}(\varepsilon_m) + \mathrm{var}(\varepsilon_s) - 2\,\mathrm{cov}(\varepsilon_m, \varepsilon_s)$.

The partial uncertainties and the corresponding correlation factors for each parameter used for the cross-section calculations for set 1 are given in table 9 and the covariance and corresponding correlation matrices for the ^{58}Ni$(n,p)^{58}$Co reaction cross-sections relative to ^{197}Au$(n,\gamma)^{198}$Au monitor reaction are given in table 10. A separate analysis was performed for each sample to monitor the combination for set 2, assuming that they are independent of each other. The partial uncertainties and the covariance (correction) matrices thus calculated for the ^{58}Ni$(n,p)^{58}$Co reaction cross-sections relative to the ^{115}In$(n,n')^{115m}$In monitor reaction at 5.99, 13.97 and 16.99 MeV neutron energies are given in tables 11 and 12, respectively. The partial uncertainties and the covariance (correction) matrices thus calculated for the ^{58}Ni$(n,2n)^{57}$Ni reaction cross-sections relative to the ^{27}Al$(n,\alpha)^{24}$Na monitor reaction at 13.97 and 16.99 MeV neutron energies are given in tables 13 and 14.

5 Theoretical framework

5.1 Calculations using the TALYS-1.9 code

The TALYS-1.9 [7] is a nuclear model code, which is used to reproduce different nuclear reaction cross-sections. The code incorporates photon, neutron, proton, deuteron, triton, ^{3}He and α-particles as the projectile on the target nuclei for incident energies up to 200 MeV. The code accounts for the effect of level density parameters, the compound and the non-compound reactions, like the pre-equilibrium and the direct reaction mechanism as a function of the incident particle energy. The code uses the Hauser-Feshbach model [60] to incorporate the effects of the compound nucleus reaction mechanism. The pre-equilibrium contribution has been included by an exciton model, which was developed by Kalbach [61]. The optical model parameters were obtained by using a global potential, which is proposed by Koning and Delaroche [62]. The TALYS-1.9 code uses the reaction parameters from the Reference Input Parameter Library (RIPL) database [63]. The TALYS-1.9 code includes all the possible outgoing reaction channels for a chosen projectile + target system. In the present analysis, six level density models (ldmodels) are incorporated in the model code for the reproduction of the nuclear reaction cross-sections. The different level densities in the TALYS code (ldmodel 1-6) account for 1) the constant temperature Fermi gas model (CTFGM) [64]; 2) back-shifted Fermi gas model (BSFGM) [65]; 3) generalised super-fluid model (GSFM) [66, 67]; 4)-5) microscopic level densities from Goriely's and Hilaire's tables [68]; and 6) microscopic level densities (temperature-dependent HFB, Gogny force) [69], respectively. Each ld-model was used and tested for the better description of the measured results. A comparison of the TALYS-1.9 code predictions with the present and the literature data are provided in figs. 5 and 7 for the ^{58}Ni$(n,p)^{58}$Co and the ^{58}Ni$(n,2n)^{57}$Ni reactions.

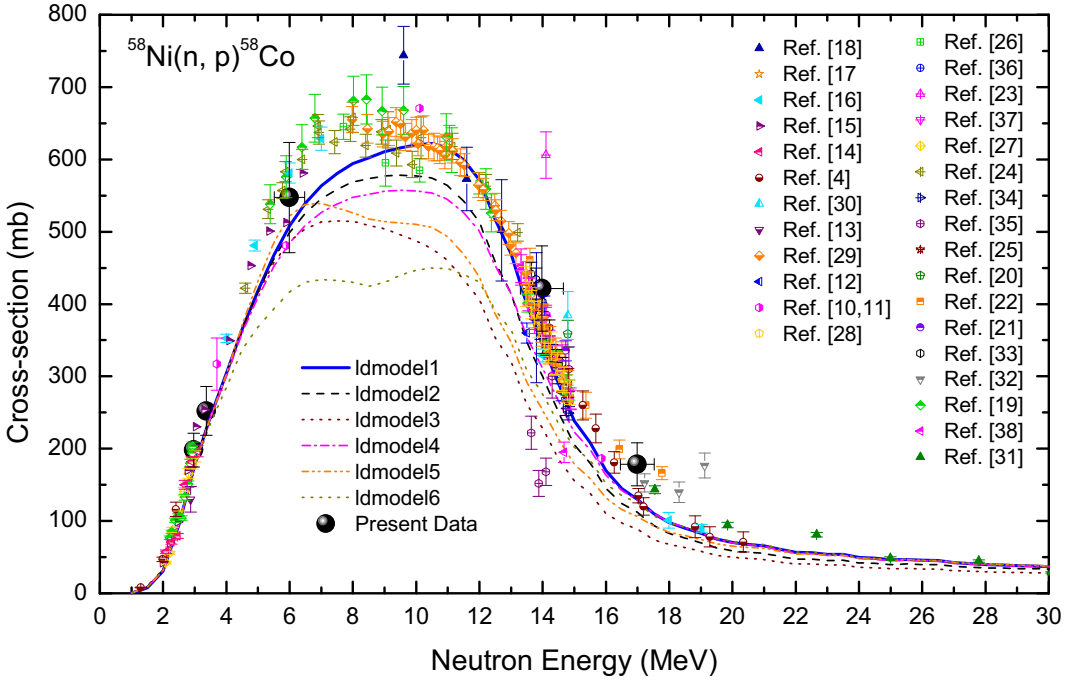

Fig. 5. (Color online) The comparison of the present data with the literature data [4, 10–38] and the theoretical reaction cross-section calculations using the TALYS-1.9 [7] code.

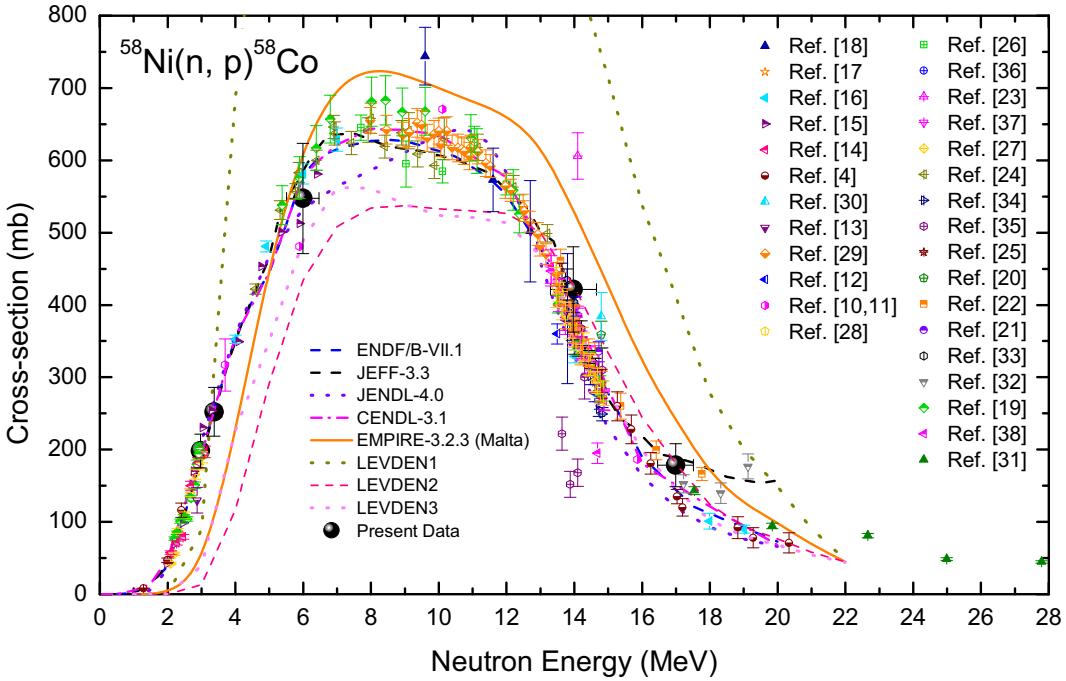

Fig. 6. (Color online)The comparison of present data with the literature data [4, 10–38], the evaluated data [56, 73–75], and the theoretical reaction cross-section calculations using the EMPIRE-3.2.2-Malta [8] code.

Table 7. Measured efficiencies with correlation matrix for the sample and the monitor reaction measured for set 1.

E_γ (keV)	Efficiency	Correlation matrix	
411.80	0.004148 ± 0.000055	1	
810.77	0.002592 ± 0.000028	0.441	1

Table 8. Measured efficiencies with correlation matrix for the sample and the monitor reaction measured for set 2.

E_γ (keV)	Efficiency	Correlation matrix		
336.241	0.051708 ± 0.000963	1		
810.77	0.025991 ± 0.000457	0.551	1	
1368.68	0.016869 ± 0.000287	0.413	0.343	1
1377.63	0.016797 ± 0.000290	0.416	0.323	0.99 1

5.2 Calculations using the EMPIRE-3.2.3-Malta code

The EMPIRE-3.2.3-Malta [8] is another code that was used to perform the calculations within the theoretical framework of some reaction model developed for the better understanding of the nuclear reaction mechanism. The EMPIRE-3.2 code works for the light particle as well as heavy-ion induced reactions for a wide range of energies. The compound nucleus reaction mechanism has been included in EMPIRE-3.2.3 by using the Hauser-Feshbach model with the width fluctuation correction [61, 70, 71]. The pre-equilibrium emission calculations can be performed by means of an exciton model or the hybrid Monte Carlo simulation approach using different optical model parameters. The code retrieves the parameters automatically from RIPL-3 data base [63]. The different level densities (LEVDEN), which can be used in the EMPIRE-3.2.3 code are: 1) the Generalised Superfluid Model [66, 67]; 2) Gilbert Cameron level densities [72]; and 3) RIPL-3 microscopic HFB level densities. EMPIRE-3.2.3 uses the Fermi Gas Model [64], which is adjusted to the RIPL-3 database for the discrete levels as the default level density (LEVDEN0) parameter. In the present work, all the level density models were tested in order to reproduce the ^{58}Ni$(n,p)^{58}$Co and the ^{58}Ni$(n,2n)^{57}$Ni reaction cross-sections for the desired energy range. The comparison of the EMPIRE-3.2.3 code predictions with the measured results and the literature data is plotted in figs. 6 and 8.

6 Results and discussions

The ^{58}Ni$(n,p)^{58}$Co and the ^{58}Ni$(n,2n)^{57}$Ni reaction cross-sections were measured using the quasi-monoenergetic neutrons based on the ^{7}Li(p,n) reaction from threshold to 18 MeV. The off-line γ-ray spectroscopic technique was used for the present measurements. Different monitor reactions, ^{197}Au$(n,\gamma)^{198}$Au, ^{115}In$(n,n')^{115m}$In and ^{27}Al$(n,\alpha)^{24}$Na, were used to calculate the neutron flux. The uncertainties from different quantities were propagated in the measured data using the covariance analysis utilizing the ratio method [53, 59]. The uncertainty due to counting statistics was found to be $\lesssim 10\%$. Other uncertainties are coming from the half-life $\lesssim 1\%$, detector dead time $\lesssim 2\%$, gamma branching ratio $\lesssim 0.01\%$, detector efficiency $\lesssim 1\%$, sample weights $\lesssim 2\%$, isotopic abundances $\lesssim 0.01\%$, monitor cross-sections $\lesssim 5\%$ and due to the self gamma absorptions $\lesssim 1\%$. The overall uncertainty in the measured cross-sections by using the covariance analysis was found within the range of 11–16%. The measured reaction cross-sections in the present work with the uncertainties calculated by using the covariance analysis are given in table 15. The present results were compared with the literature data [4,10–46] as well as with the theoretically calculated data using the TALYS-1.9 [7] and the EMPIRE-3.2.3-Malta [8] nuclear codes. The evaluated data libraries, like ENDF/B-VII.1 [56], JENDL-4.0 [73], CENDL-3.1 [74], and JEFF-3.2 [75] were also used for the comparison of the present results. In general, the present data were found in fairly good agreement with the literature, the theoretical model predictions and the evaluated data. However, a detailed discussion on the results is provided in the following subsections.

6.1 The ^{58}Ni(n, p)^{58}Co reaction

The ^{58}Ni(n,p) reaction cross-sections were measured at two neutron energies, 2.97 ± 0.19, and 3.37 ± 0.23 MeV relative to the ^{197}Au$(n,\gamma)^{198}$Au monitor cross-sections, and at three neutron energies, 5.99 ± 0.48, 13.97 ± 0.68, and 16.99 ± 0.53 MeV relative to the ^{115}In$(n,n')^{115m}$In monitor cross-sections, respectively. The comparison of the results with the literature [4, 10–38] and the data from the TALYS-1.9 [7] theoretical model calculations using various level density models is shown in fig. 5. An enormous amount of data is available in the literature [4, 10–38] for the ^{58}Co production using the ^{58}Ni targets. It can be seen from fig. 5 that most of the data are, however, concentrated around the 14 MeV neutron energies with minor discrepancies. A few from data [10, 18, 19, 26] were found slightly enhanced as compared to the rest of the cross-section data. The enhancement in the cross-sections may be due to the use of the different monitor reaction cross-sections. Disagreement in the results among different authors [23, 32, 35] has been found to be more around the 13–22 MeV neutron energies. However, the present data were found to be in accordance with the literature data [4,10–46]. Different ldmodels available in the TALYS-1.9 code were also tested for the present case. As can be seen from the figure, the Fermi gas model (ldmodel1) [64], which is the default input for any projectile+target system, has been found most suitable for the reproduction of the measured data. The data from different ldmodels were found in general agreement in the entire energy range of neutron energies except around the peak at 10 MeV. For the sake of clarity, the comparison of the ^{58}Ni$(n,p)^{58}$Co reaction cross-section data with the evaluated and the theoretical reproductions from the EMPIRE-3.2.3-Malta [8] code were plotted in a separate fig. 6. It can be observed from fig. 6 that the present as well as

Table 9. Fractional uncertainties in various parameters used to obtain ^{58}Ni$(n,p)^{58}$Co reaction cross-sections.

E_n (MeV)	Partial uncertainty (%)												
	C_s	C_m	I_{γ_s}	ε_s	ε_m	f_{λ_s}	f_{λ_m}	M_s	M_m	a_s	A_r	A_m	σ_W
2.97 ± 0.19	10.874	2.932	0.00905	1.0819	1.342	0.0962	0.0054	1.881	2.595	0.0132	1.208E-06	3.030E-07	1.007
3.37 ± 0.23	8.962	9.433	0.00905	1.0891	1.342	0.0923	0.0071	1.562	2.149	0.0132	1.208E-06	3.030E-0	0.862
Corr	0	0	1	1	1	1	1	0	0	1	1	1	0

Table 10. Covariance matrix (%) and corresponding correlation coefficients for the measured ^{58}Ni$(n,p)^{58}$Co reaction cross-sections using the FOTIA at BARC.

E_n (MeV)	Covariance matrix ($V_{cs_{ij}}$)	Correlation matrix	
2.97 ± 0.19	1.4113	1	
3.37 ± 0.23	0.0298	1.8011	0.0187	1

the literature data agree with each other for the entire range of neutron energies under consideration. On the other hand, only the default input description uses the Fermi gas model [64] (LEVDEN0). In the EMPIRE-3.2.3-Malta while using LEVDEN0 it was found successful to reproduce the trend of the cross-section data. From figs. 5 and 6, it can be stated that the TALYS-1.9 [7] code's input descriptions were found better than the EMPIRE-3.2.3-Malta [8] results in order to reproduce the ^{58}Ni$(n,p)^{58}$Co reaction cross-sections.

6.2 The ^{58}Ni(n, 2n)^{57}Ni reaction

The ^{58}Ni$(n,2n)$ reaction cross-sections were measured at only two neutron energies, 13.97 ± 0.68, and 16.99 ± 0.53 MeV relative to the ^{27}Al$(n,\alpha)^{24}$Na monitor cross-sections. The comparison of the present, literature and the theoretical data using the TALYS-1.9 code [7] is plotted in fig. 7. Most of the literature data [4, 28–45] were found to be concentrated around 14 MeV. The data [4, 30, 32, 35, 39, 40, 46] above 15 MeV were found to have minor discrepancies. The trend of the data above 15 MeV again suggests the disagreement among the data from different authors [4, 32, 35, 39, 40, 46], which may be attributed to the use of different monitor cross-sections. On the other hand, the present data were found in agreement with the literature data except those given in refs. [30, 39, 40, 46]. The ^{27}Al$(n,\alpha)^{24}$Na monitor reaction cross-sections contains $\approx 2.5\%$ uncertainty [56] around 16 MeV neutron energies, therefore, large uncertainty can be observed in the ^{57}Ni production cross-section at 16.99 ± 0.53 MeV neutron energy. It can also be observed from fig. 7 that the level density models ldmodel 1-3 [64–67] were found successful in order to reproduce the experimental results having better agreement with ldmodel 1 and 2. Similarly, a comparison of the present and the literature data with the evaluated and the theoretical data using the EMPIRE-3.2.3-Malta code are plotted in fig. 8. From the figure, it can be noted that the evaluated data able to describe the literature data in the entire range of energies, however, none of the level density model from the EMPIRE code was found successful to reproduce the experimental values of the reaction cross-sections. Figures 7 and 8 show that the results from TALYS and EMPIRE using the similar level density model (Fermi gas model) disagree for the neutron energies above 14 MeV. The larger cross-sections from the EMPIRE code may arise due to the over prediction of the compound nucleus formation over the pre-equilibrium process. Therefore, it can be stated that the TALYS-1.9 [7] predictions were found more accurate for the reproduction of the neutron-induced reaction cross-section data.

The CN and PE are the most dominated reaction channels at the present energies of investigation, therefore, these two channels contributes majorly in the total reaction cross-section with minor contribution coming from the direct reactions. To further investigate the role of the PE process in the formation of the ^{58}Co and ^{57}Ni radioisotopes, the theoretical reaction cross-section was calculated by switching off the PE contribution in both the TALYS-1.9 and EMPIRE-3.2.3-Malta codes. A comparison among the present, literature and the theoretical cross-section data from TALYS-.9 and EMPIRE-3.2.3-Malta has been presented for ^{58}Ni$(n,p)^{58}$Co and ^{58}Ni$(n,2n)^{57}$Ni reactions in figs. 9 and 10, respectively. The mean free path parameter (MFP) has been tested with different sets of values and together with the different optical model potentials to properly fit the data. A better fit can be found by changing certain parameters in the code. However, the best fit found by switching off the PE process in the calculations is successfully describing the results. It can be seen from fig. 9 that the TALYS-1.9 code was found to be successful in order to reproduce the reaction cross-section data. On the other hand, the data from the EMPIRE-3.2.3-Malta code were found to be more enhanced after switching off the PE calculations in the input description of the code. However, both codes were found successful in order to fit the data more accurately without the PE contribution for the ^{58}Ni$(n,2n)^{57}$Ni reaction, as can be seen from fig. 10. Both figs. 9 and 10 show that the default input description of the theoretical model code EMPIRE-3.2.3-Malta is over-predicting either the CN or PE contribution in the production of the ^{58}Co and ^{57}Ni radioisotopes, which may be attributed to the default value of MFP = 1.5 of the code.

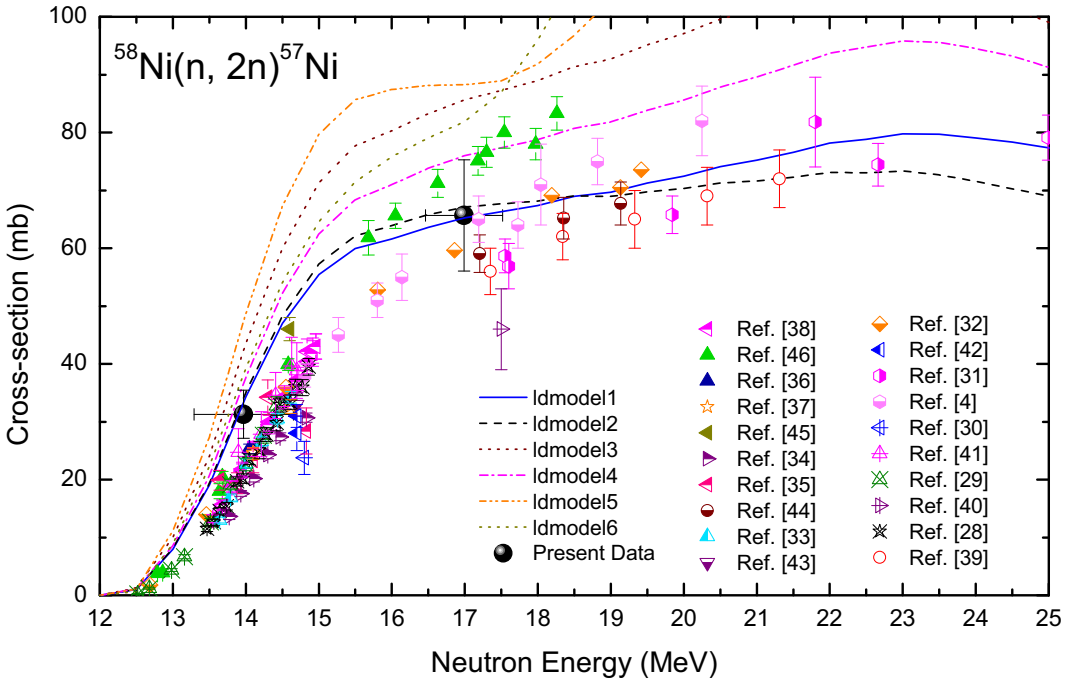

Fig. 7. (Color online) The comparison of the present data with the literature data [4, 28–45] and the theoretical reaction cross-section calculations using the TALYS-1.9 [7] code.

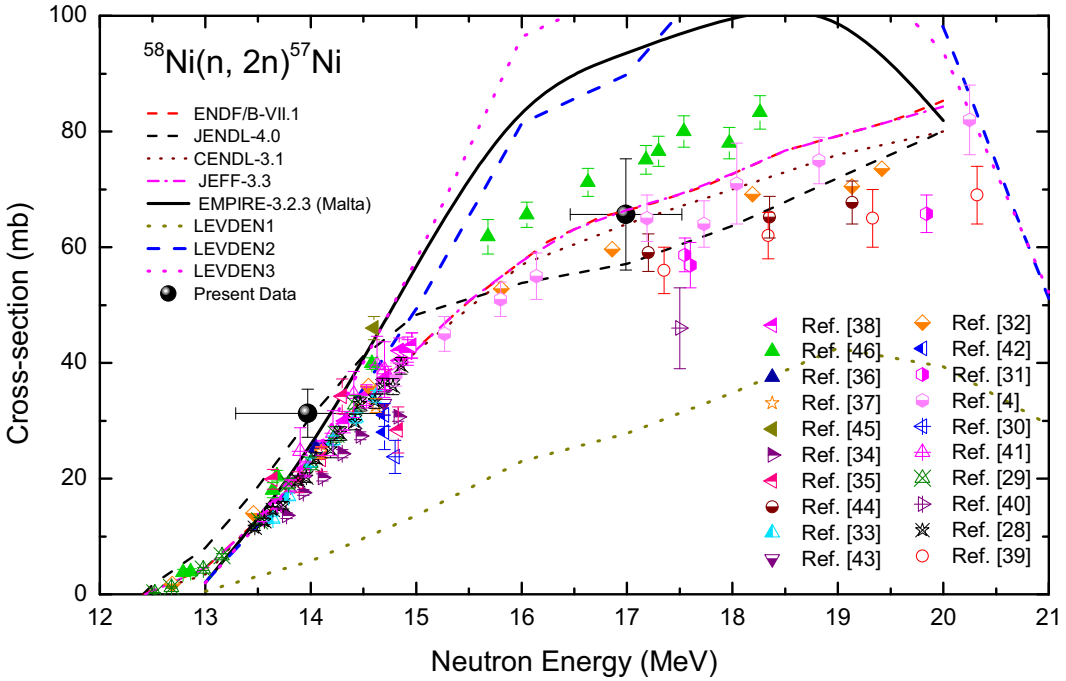

Fig. 8. (Color online) The comparison of the present data with the literature data [4, 28–45], the evaluated data [56, 73–75], and the theoretical reaction cross-section calculations using the EMPIRE-3.2.2-Malta [8] codes.

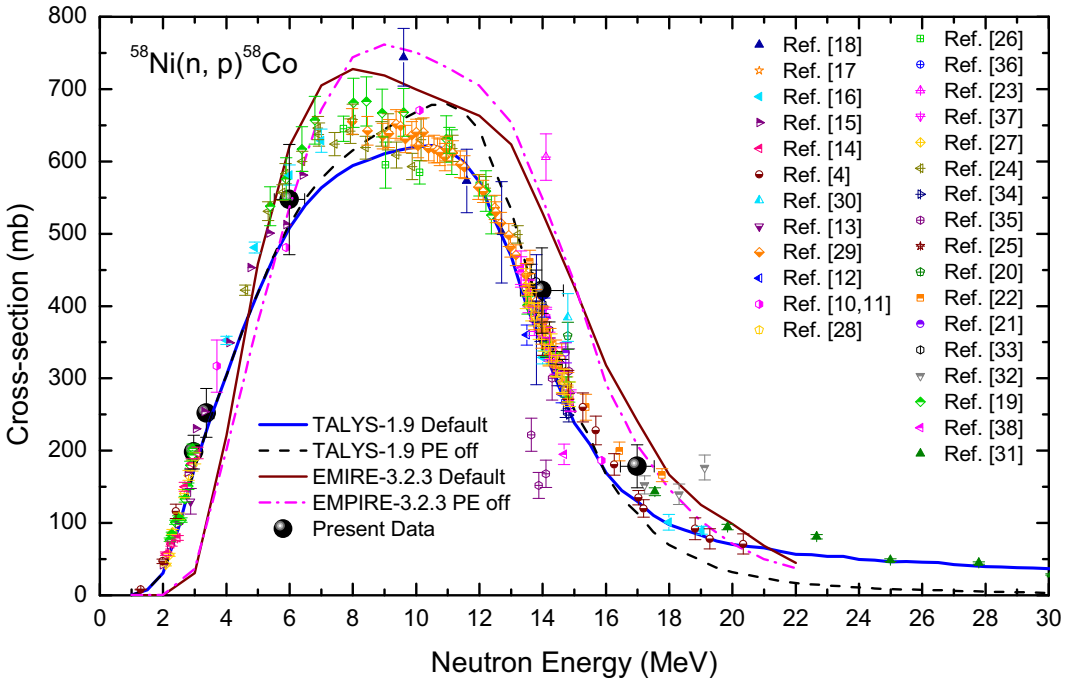

Fig. 9. (Color online) The comparison of the present data with the literature data [4,10–38], and the theoretical reaction cross-section calculations (default and by switching off the PE contribution) using the TALYS-1.9 [7] and EMPIRE-3.2.2-Malta [8] codes.

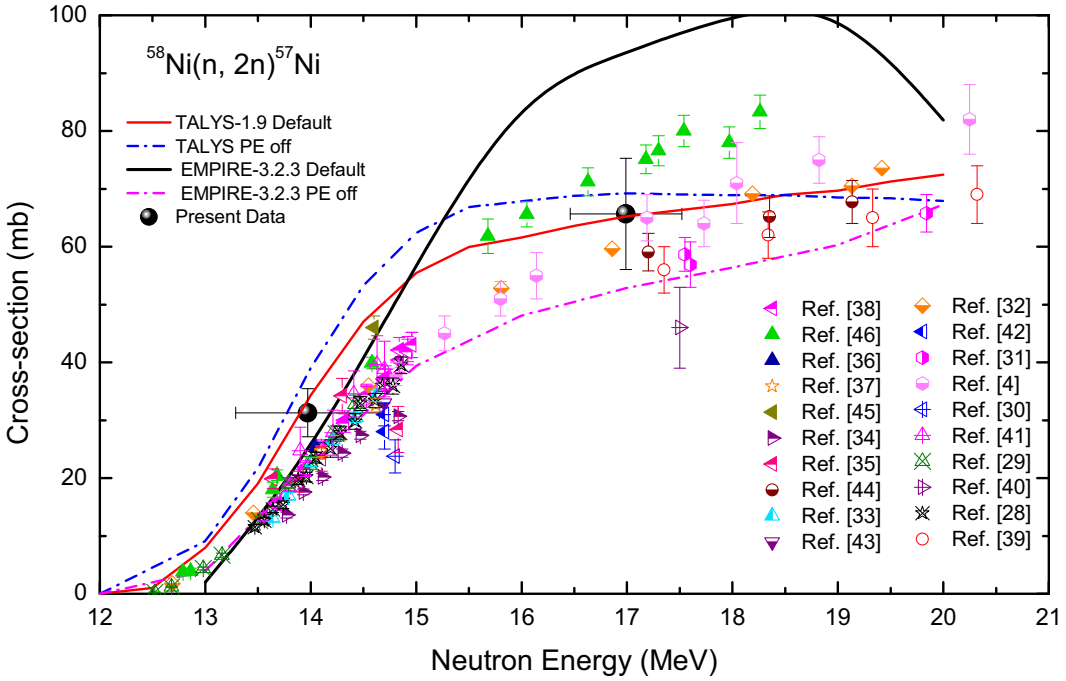

Fig. 10. (Color online) The comparison of the present data with the literature data [4,28–45]and the theoretical reaction cross-section calculations (default and by switching off the PE contribution) using the TALYS-1.9 [7] and EMPIRE-3.2.2-Malta [8] code.

Table 11. Fractional uncertainties in various parameters used to obtain ^{58}Ni$(n,p)^{58}$Co reaction cross-sections.

E_n (MeV)	Partial uncertainty (%)												
	C_s	C_m	I_{γ_s}	I_{γ_m}	$\eta_{m,s}$	f_{λ_s}	f_{λ_m}	M_s	M_m	a_s	A_r	A_m	σ_W
5.99 ± 0.48	8.747	8.932	0.00905	0.217	0.0405	0.0950	0.000186	1.641	1.595	0.0132	1.20E-06	4.35E-06	5.67
13.97 ± 0.68	9.962	7.433	0.00905	0.217	0.0405	0.0968	0.000793	1.462	2.489	0.0132	1.20E-06	4.35E-06	5.67
16.99 ± 0.53	11.923	9.934	0.00905	0.217	0.0405	0.0973	0.000601	1.280	1.995	0.0132	1.20E-06	4.35E-06	5.67
Corr	0	0	1	1	1	1	1	0	0	1	1	1	0

Table 12. Covariance matrix (%) and corresponding correlation coefficients for the measured ^{58}Ni$(n,p)^{58}$Co reaction cross-sections using the BARC-TIFR Pelletron facility.

E_n (MeV)	Covariance matrix ($V_{cs_{ij}}$)			Correlation matrix		
5.99 ± 0.48	1.9375			1		
13.97 ± 0.68	0.3221	1.9698		0.164	1	
16.99 ± 0.53	0.3221	0.3221	2.79614	0.138	0.1371	1

Table 13. Fractional uncertainties in various parameters used to obtain ^{58}Ni$(n,2n)^{57}$Ni reaction cross-sections.

E_n (MeV)	Partial uncertainty (%)												
	C_s	C_m	I_{γ_s}	I_{γ_m}	$\eta_{m,s}$	f_{λ_s}	f_{λ_m}	M_s	M_m	a_s	A_r	A_m	σ_W
13.97 ± 0.68	9.248	8.849	0.293	0.0015	0.00105	0.00058	0.0015	1.28	1.495	0.0132	1.21E-06	4.45E-07	0.37
16.99 ± 0.53	10.122	10.161	0.293	0.0015	0.00105	0.0021	0.0018	1.162	1.049	0.0132	1.21E-06	4.45E-07	2.03
Corr	0	0	1	1	1	1	1	0	0	1	1	1	0

Table 14. Covariance matrix (%) and corresponding correlation coefficients for the measured ^{58}Ni$(n,2n)^{57}$Ni reaction cross-sections using the BARC-TIFR Pelletron facility.

E_n (MeV)	Covariance matrix ($V_{cs_{ij}}$)		Correlation matrix	
13.97 ± 0.68	1.7774	1		
16.99 ± 0.53	8.65×10^4	2.3594	0.0004	1

7 Summary and conclusions

1) The ^{58}Co and the ^{57}Ni production cross-sections for different quasi-monoenergetic neutrons produced from the ^{7}Li(p,n) reaction were measured by using the off-line γ-ray spectroscopic technique.
2) Detailed covariance analysis was used to calculate the uncertainties and the correlations among the measured cross-sections and was found within the range of 11–16%.
3) The present results were found in agreement with the literature as well as with the evaluated data from data libraries like ENDF/B-VII.1, JENDL-4.0, CENDL-3.1, and JEFF-3.2.
4) From the present study of the two nuclear model codes TALYS-1.9 and EMPIRE-3.2.3-Malta, it can be stated that the TALYS-1.9 was found better in order to reproduce the neutron-induced reaction cross-section data. It can also be stated that no significant role of the PE process was found up to 20 MeV neutron energies in the production cross-sections of ^{58}Co and ^{57}Ni radioisotopes.
5) The disagreement between the two codes may be attributed to the over-prediction of CN/PE contributions. The present study presents a clear insight into both the nuclear model code and is also useful for the validation of the literature data within the considered neutron energies.
6) The monitor reaction cross-sections can produce large uncertainties in the measured data, therefore, the error propagation techniques are recommended to estimate the correlations among the cross-sections.
7) The present work is also vital for the advancement of nuclear reactor and medical accelerator technology and for the dose estimation of the medical isotope ^{58}Co.

One of the authors (SM) thanks the Department of Atomic Energy-Board of Research in Nuclear Sciences (DAE-BRNS)

Table 15. The measured cross-sections for the ^{58}Ni$(n,p)^{58}$Co and ^{58}Ni$(n,2n)^{57}$Ni reactions.

Neutron energy	^{58}Ni$(n,p)^{58}$Co		^{58}Ni$(n,2n)^{57}$Ni	
	Flux	Cross-section	Flux	Cross-section
(MeV)	(n cm^{-2} s^{-1})	(mb)	(n cm^{-2} s^{-1})	(mb)
2.97 ± 0.19	3.5×10^6	198.07 ± 23.37	–	–
3.37 ± 0.23	3.8×10^6	252.21 ± 33.79	–	–
5.99 ± 0.48	2.4×10^6	547.32 ± 76.07	–	–
13.97 ± 0.68	3.2×10^6	421.29 ± 58.98	1.48×10^6	31.28 ± 4.16
16.99 ± 0.53	6.05×10^6	178.47 ± 29.8	2.68×10^6	65.67 ± 9.59

for the sanction of a major research project (Sanction Number: 36(6)/14/22/2016-BRNS) as well as providing fellowship to the author (SP). The authors are thankful to Prof. V. Nanal, Mr. Anil Shanbag and the staff of the Pelletron facility Tata Institute of Fundamental Research (TIFR), Mumbai for their excellent operation of the accelerator and other supports during the experiment. The authors are also thankful to Dr. K. Katovsky, Department of Electrical Power Engineering, Brno University of Technology, Brno, Czech Republic for performing MCNP6.1 calculations for neutron spectra generation.

Data Availability Statement This manuscript has no associated data or the data will not be deposited. [Authors' comment: All the data generated during this study are contained in this article.]

Publisher's Note The EPJ Publishers remain neutral with regard to jurisdictional claims in published maps and institutional affiliations.

References

1. C. Rubbia, J.A. Rubio, S. Buono, F. Carminati, N. Fietier, J. Galvez, C. Geles, Y. Kadi, R. Klapisch, P. Mandrilion, J.P. Revol, Ch. Roche, *Conceptual Design of a Fast Neutron Operated High Power Energy Amplifier*, CERN Report No. CERN/AT/95-44 (ET) (1995).
2. C.D. Bowman, Annu. Rev. Nucl. Part. Sci. **48**, 505 (1998).
3. U. Fischer, P. Batistoni, E. Cheng, R.A. Forrest, T. Nishitani, AIP Conf. Proc. **769**, 1478 (2005).
4. V. Semkova, V. Avrigeanu, T. Glodariu, A.J. Koning, A.J.M. Plompen, D.L. Smith, S. Sudar, Nucl. Phys. A **730**, 255 (2004).
5. C.L. Whitmarsh, Oak Ridge National Laboratory Report: ORNL-3281, UC-80-Reactor technology, TID-4500, 17th ed.
6. D.L. Mollin, Proc. R. Soc. Med. **55**, 141 (1962).
7. A.J. Koning, S. Hilaire, S. Goriely, *TALYS user manual, A nuclear reaction program*, NRG-1755 ZG PETTEN (The Netherlands, 2015).
8. M. Herman, R. Capote, M. Sin, A. Trkov, B.V. Carlson, P. Oblozinsksy, C.M. Mattoon, H. Wienkey, S. Hoblit, Young-Sik Cho, G.P.A. Nobre, V.A. Plujko, V. Zerkin, *EMPIRE-3.2 Malta modular system for nuclear reaction calculations and nuclear data evaluation*, user manual, INDC(NDS)-0603, BNL-101378-2013 (2014).
9. EXFOR, NDS-120, (2014) pp. 272–276, `https://www-nds.iaea.org/exfor/exfor.htm`.
10. B.S. Shivashankar, H. Naik, N. Sreekumaran Nair, S. Ganesan, S.V. Suryanarayana, K. Manjunatha Prasad, Nucl. Sci. Eng. **179**, 423 (2015).
11. B.S. Shivashankar H. Naik, S.V. Suryanarayana, P.M. Prajapati, V.K. Mulik, K.C. Jagadeesan, S.V. Thakare, A. Goswami, S. Ganesan, J. Radioanal. Nucl. Chem. **292**, 745 (2012).
12. F. Zhou, Xiajie Xiao, Kaihong Fang, Changlin Lan, Xiangzhong Kong, Nucl. Instrum. Methods Phys. Res. B **269**, 642 (2011).
13. M. Bhike, A. Saxena, B.K. Nayak, S. Ganesan, B. Lalremruata, R. Palit, R. Tripathi, S. Sodaye, A.V.R. Reddy, S. Kailas, R.K. Choudhury, *Conference on Nuclear Data for Advanced Nuclear Systems, Mangalore, India, 2006* (2006) p. TP15.
14. T. Shimizu, H. Sakane, M. Shibata, K. Kawade, T. Nishitani, Ann. Nucl. Energy **31**, 975 (2004).
15. T. Senga, H. Sakane, M. Shibata, H. Yamamoto, K. Kawade, Y. Kasugai, Y. Ikeda, H. Takeuchi, T. Furuta, Japanese report to the I.N.D.C., No. 185/U (2000).
16. Xiaolong Huang, Weixiang Yu, Xiaogang Han, Wenrong Zhao, Hanlin Lu, Jinxiang Chen, Zhaomin Shi, Gouyou Tang, Guohui Zhang, Nucl. Sci. Eng. **131**, 267 (1999).
17. V. Avrigeanu, S. Sudar, Cs.M. Buczko, J. Csikai, A.A. Filatenkov, S.V. Chuvaev, R. Doczi, V. Semkova, V.A. Zelenetsky, Phys. Rev. C **60**, 017602 (1999).
18. J.C. Suita, A.G. da Silva, L.T. Auler, S. de Barros, Nucl. Sci. Eng. **126**, 101 (1997).
19. Cs.M. Buczko, J. Csikai, S. Sudar, A. Grallert, S.A. Jonah, B.W. Jimba, T. Chimoye, M. Wagner, Phys. Rev. C **52**, 1940 (1995).
20. I. Garlea, Chr. Miron-Garlea, H.N. Rosu, G. Fodor, V. Raducu, Rev. Roum. Phys. **37**, 19 (1992).
21. M. Belgaid, M. Siad, M. Allab, J. Radioanal. Nucl. Chem. Lett. **166**, 493 (1992).
22. Li Tingyan, Shi Zhaomin, Lu Hanlin, Zhao Wenrong, Yu Weixiang, Yuan Xialin, High Energy Phys. Nucl. Phys. **16**, 151 (1992) (Chinese ed.).
23. L.I. Klochkova, B.S. Kovrigin, V.N. Kuritsin, Rept: USSR report to the I.N.D.C., No. 376 (1994).
24. D.L. Smith, J.W. Meadows, H. Vonach, M. Wagner, R.C. Haight, W. Mannhart, *Conference on Nuclear Data for Science and Technology, Juelich 1991* (1991) p. 282.
25. P.M. Dighe, G.R. Pansare, R. Sarkar, V.N. Bhoraskar, J. Phys. G **17**, L169 (1991).
26. H. Vonach, M. Wagner, R.C. Haight, *Nuclear Energy Agency Nuclear Data Committee reports*, No. 259 (1990) p. 165.

27. Y. Ikeda, C. Konno, K. Kosako, K. Oishi, Japanese report to NEANDC, No. 155 (1990) p. 11.
28. A.A. Filatenkov, Rept: USSR report to the I.N.D.C., No. 0460 (2016) https://www-ds.iaea.org/publications/indc/indc-ccp-0460/.
29. W. Mannhart, D. Schmidt, AIP Conf. Proc. **769**, 609 (2005).
30. A.K.M. Harun-Ar-Rashid, M.U. Khandaker, M.N. Islam, A.K.M.M.H. Meaze, Sk.A. Latif, M.A. Halim, K. Naher, M.N. Chowdhury, M.S. Uddin, M.A. Hafiz, M.M. Rahman, Indian J. Phys. **80**, 737 (2006).
31. Y. Uno, S. Meigo, S. Chiba, T. Fukahori, Y. Kasugai, O. Iwamoto, P. Siegler, Y. Ikeda, *9th International Symposium on Reactor Dosimetry, Prague* (1996) p. 465.
32. S. Iwasaki, M. Sakuma, K. Sugiyama, N. Odano, JAERI-M Reports, No. 93-046 (1993) p. 257.
33. Yuan Junqian, Wang Yongchang, Kong Xiangzhong, Yang Jingkang, High Energy Phys. Nucl. Phys. **16**, 57 (1992) (Chinese ed.).
34. M. Viennot, M. Berrada, G. Paic, S. Joly, Nucl. Sci. Eng. **108**, 289 (1991).
35. N.I. Molla, R.U. Miah, M. Rahman, Aysha Akhter, *Conference on Nuclear Data for Science and Technology, Juelich 1991* (1991) p. 355.
36. I. Kimura, K. Kobayashi, Nucl. Sci. Eng. **106**, 332 (1990).
37. Li Guozheng, Jiang Jinghe, High Energy Phys. Nucl. Phys. **14**, 1023 (1990) (Chinese ed.).
38. Y. Ikeda, C. Konno, K. Oishi, T. Nakamura, H. Miyade, K. Kawade, H. Yamamoto, T. Katoh, JAERI Reports, No. 1312 (1988).
39. B. Champine, M.E. Gooden, Krishichayan, E.B. Norman, N.D. Scielzo, M.A. Stoyer, K.J. Thomas, A.P. Tonchev, W. Tornow, B.S. Wang, Phys. Rev. C **93**, 014611 (2016).
40. J. Vrzalova, O. Svoboda, A. Krasa, A. Kugler, M. Majerle, M. Suchopar, V. Wagner, Nucl. Instrum. Methods Phys. Res., Sect. A **726**, 84 (2013).
41. M.A. Hafiz, Indian J. Pure Appl. Phys. **45**, 425 (2007).
42. K.T. Osman, F.I. Habbani, Rept: Sudanese report to the I.N.D.C., No. 001 (1996).
43. G.R. Pansare, V.N. Bhoraskar, Int. J. Mod. Phys., Part E **2**, 259 (1993).
44. M. Sakuma, S. Iwasaki, H. Shimada, N. Odano, K. Suda, J.R. Dumais, K. Sugiyama, JAERI-M Reports, No. 92-027 (1992) p. 278.
45. A. Ercan, M.N. Erduran, M. Subasi, E. Gueltekin, G. Tarcan, A. Baykal, M. Bostan, *Conference on Nuclear Data for Science and Technology, Juelich 1991* (1991) p. 376.
46. Lu Hanlin, Huang Jianzhou, Fan Peiguo, Cui Yunfeng, Zhao Wenrong, Chinese report to the I.N.D.C., No. 16 (1989).
47. J.F. Ziegler, Nucl. Instrum. Methods B **219**, 1027 (2004).
48. *Chart of Nuclides* (National Nuclear Data Center, Brookhaven National Laboratory) https://www.nndc.bnl.gov/chart/.
49. H. Liskien, A. Paulsen, At. Data Nucl. Data Tables **15**, 57 (1975).
50. J.W. Meadows, D.L. Smith, *Neutrons from Proton Bombardment of Natural Lithium*, Argonne National Laboratory Report ANL-7983 (1972).
51. C.H. Poppe, J.D. Anderson, J.C. Davis, S.M. Grimes, C. Wong, Phys. Rev. C **14**, 438 (1976).
52. H. Naik, P.M. Prajapati, S.V. Surayanarayana, K.C. Jagadeesan, S.V. Thakare, D. Raj, V.K. Mulik, B.S. Sivashankar, B.K. Nayak, S.C. Sharma, S. Mukherjee, Sarbjit Singh, A. Goswami, S. Ganesan, V.K. Manchanda, Eur. Phys. J. A **47**, 51 (2011).
53. S. Parashari, S. Mukherjee, A.P. Singh, Vibha Vansola, H. Naik, B.K. Nayak, Rajnikant Makwana, S.V. Suryanarayana, N.L. Singh, Mayur Mehta, Y.S. Sheela, M. Karkera, R.D. Chauhan, S.C. Sharma, Phys. Rev. C **98**, 014625 (2018).
54. R. Makwana, S. Mukherjee, P. Mishra, H. Naik, N.L. Singh, M. Mehta, K. Katovsky, S.V. Suryanarayana, V. Vansola, Y. Santhi Sheela, M. Karkera, R. Acharya, S. Khirwadkar, Phys. Rev. C **96**, 024608 (2017).
55. *NuDat* 2.7β (National Nuclear Data Center, Brookhaven National Laboratory, 2011) http://www.nndc.bnl.gov/.
56. *ENDF/B-VII.1* (National Nuclear Data Center, Brookhaven National Laboratory, 2011) http://www.nndc.bnl.gov/exfor/endf00.jsp.
57. *IAEA-EXFOR experimental nuclear reaction data base*, http://www.nds.iaea.org/exfor.
58. T. Vidmar, G. Kanish, G. Vidmar, Appl. Rad. Isot. **69**, 908 (2011).
59. N. Otuka, B. Lalremruata, M.U. Khandaker, A.R. Usmand, L.R.M. Punte, Radiat. Phys. Chem. **502**, 140 (2017).
60. W. Hauser, H. Feshbach, Phys. Rev. **87**, 366 (1952).
61. C. Kalbach, Phys. Rev. C **33**, 818 (1986).
62. A.J. Koning, J.P. Declaroche, Nucl. Phys. A **713**, 231 (2003).
63. R. Capote, M. Herman, P. Obložinský, P.G. Young, S. Goriely, T. Belgya, A.V. Ignatyuk, A.J. Koning, S. Hilaire, V.A. Plujko, M. Avrigeanu, O. Bersillon, M.B. Chadwick, T. Fukahori, Zhigang Ge, Yinlu Han, S. Kailas, J. Kopecky, V.M. Maslov, G. Reffo, M. Sin, E.Sh. Soukhovitskii, P. Talou, Nucl. Data Sheets **110**, 3107 (2009).
64. A. Gilbert, A.G.W. Cameron, Can. J. Phys. **43**, 1446 (1965).
65. W. Dilg, W. Schantl, H. Vonach, M. Uhl, Nucl. Phys. A **217**, 269 (1973).
66. A.V. Ignatyuk, K.K. Istekov, G.N. Smirenkin, Sov. J. Nucl. Phys. **29**, 450 (1979).
67. A.V. Ignatyuk, J.L. Weil, S. Raman, S. Kahane, Phys. Rev. C **47**, 1504 (1993).
68. S. Goriely, S. Hilaire, A.J. Koning, Phys. Rev. C **78**, 064307 (2008).
69. S. Hilaire, M. Girod, S. Goriely, A.J. Koning, Phys. Rev. C **86**, 064317 (2012).
70. H.M. Hofmann, J. Richert, J.W. Tepel, H.A. Weidenmuller, Ann. Phys. **90**, 403 (1975).
71. A. Adam, L. Jeki, Acta Phys. Acad. Sci. Hung. **26**, 335 (1969).
72. A.S. Ilijinov *et al.*, Nucl. Phys. A **534**, 517 (1992).
73. K. Shibata, O. Iwamoto, T. Nakagawa, N. Iwamoto, A. Ichihara, S. Kunieda, S. Chiba, K. Furutaka, N. Otuka, T. Ohasawa, T. Murata, H. Matsunobu, A. Zukeran, S. Kamada, J. Nucl. Sci. Technol. **48**, 1 (2011).
74. Z.G. Ge, Z.X. Zhao, H.H. Xia, Y.X. Zhuang, T.J. Liu, J.S. Zhang, H.C. Wu, J. Kor. Phys. Soc. **59**, 1052 (2011).
75. A.J. Koning, E. Bauge, C.J. Dean, E. Dupont, U. Fischer, R.A. Forrest, R. Jacqmin, H. Leeb, M.A. Kellet, R.W. Mills, C. Nordborg, M. Pescarini, Y. Rugama, P. Rullhusen, J. Kor. Phys. Soc. **59**, 1057 (2011).